INL/RPT-XX-XXXX

Hybrid physics-based and machine learning tools for materials assessment

September 2023

William Tanner Yorgason[1], Mathew Swisher[1], and Andrea Jokisaari[1]

[1]*Idaho National Laboratory*

Idaho National Laboratory

INL is a U.S. Department of Energy National Laboratory
operated by Battelle Energy Alliance, LLC

INL/RPT-XX-XXXX

Hybrid physics-based and machine learning tools for materials assessment

William Tanner Yorgason[1], **Mathew Swisher**[1], **and Andrea Jokisaari**[1]

[1]**Idaho National Laboratory**

September 2023

Idaho National Laboratory
Idaho Falls, Idaho 83415

http://www.inl.gov

Prepared for the
U.S. Department of Energy
Office of Nuclear Energy
Under DOE Idaho Operations Office
Contract DE-AC07-05ID14517

Page intentionally left blank

SUMMARY

[Andrea to supply something here]

ACKNOWLEDGEMENTS

This research made use of the resources of the High Performance Computing Center at Idaho National Laboratory, which is supported by the Office of Nuclear Energy of the U.S. Department of Energy and the Nuclear Science User Facilities under Contract No. DE-AC07-05ID14517.

Page intentionally left blank

CONTENTS

SUMMARY iii

ACKNOWLEDGEMENTS iv

1 INTRODUCTION 1

1.1 TANNER'S INTRO 1

1.2 MATHEW'S INTRO 2

2 Machine Learning and Density Functional Theory 3

2.1 Methods 3

2.1.1 Density Functional Theory 3
2.1.2 Machine Learned Nudged Elastic Band 4
2.1.3 Ising Model 5
2.2 Results 5

2.2.1 Face Centered Cubic Iron 5
2.2.2 Stainless Steel 316 6
2.3 Impact 8

3 Molecular Dynamics of Collision Cascades in Metals 8

3.1 Methods 8

3.1.1 Molecular Dynamics Models 8
3.1.2 Collision Cascade Simulations 9
3.2 Results 10

3.2.1 Peak Cascade Damage 12
3.2.2 Recombination and Spontaneous Recombination Distance 13

4 CONCLUSIONS 14

4.1 TANNERS CONCLUSION 16

4.2 MATHEWS CONCLUSION 16

REFERENCES 17

FIGURES

Figure 1. Ising model results for FCC Fe. The T_C of pristine FCC Fe [1] is approximated and ferromagnetism is predicted well beyond this temperature when a vacancy is present. 6
Figure 2. Energy pathway for vacancy diffusion in FCC Fe, showing both FM and NM cases. Image number refers to the images or spatial configuration of the atoms as the vacancy diffuses from one site to another. 7
Figure 3. Ising model results for SS-316. Ferromagnetism is predicted well beyond this temperature when a vacancy is present, regardless vacancy's nearest neighbors. ... 8
Figure 4. Energy pathway for vacancy diffusion in SS-316. Legend shows the species which diffuses opposite the vacancy. Image number refers to the images or spatial configuration of the atoms as the vacancy diffuses from one site to another. 9
Figure 5. The average time evolution of cascade-created Frenkel pairs in Al, Ni, Fe, Cu, and Mo. Each profile shown is the average of 10 simulations. 11
Figure 6. Relation between maximum cascade size and the initial mach number of the PKA. Linear regression shown has $R^2 = 0.93$ 13
Figure 7. A schematic representation of the SRD and the recombination radius (R_r). White circles represent individual vacancies and red circles represent individual interstitials. (a) The spontaneous recombination distance in a collision cascade. The blue region represents the cascade core, which is rich in vacancies, and the red region represents the region rich in displaced atoms that forms an interstitial shell. (b) The recombination radius is calculated by treating the vacancy as a spherical sink with a radius, R_r, that will capture and recombine with a diffusing interstitial and result in a perfect crystal lattice. The distance between the interstitial and vacancy is referred to as the recombination radius. 14

Page intentionally left blank

1. INTRODUCTION

[Please write individual section introductions and Andrea can massage them together.]

1.1 TANNER'S INTRO

Nuclear energy has several key advantages, such as low CO_2 emissions, high reliability, and the potential to recycle spent fuel [2–5]. However, irradiation damage in structural materials limits nuclear energy's potential, requiring part replacement and therefore increasing cost. This becomes even more important as advanced reactors are implemented because they require higher temperatures and higher neutron fluxes [6]. Irradiation damage can, however, be mitigated by several methods. Thus we briefly review irradiation damage and then discuss one method for its mitigation.

Irradiation damage begins with the collision of a high energy particle (i.e., neutron) with an atom in a material. This interaction transfers kinetic energy from this atom to others, cascading to destroy material's atomic lattice. While most of this lattice damage is annealed due to the resulting high local temperature of the cascade region, vacancies and other defects remain. The vacancies then, given the high ambient temperature nuclear reactor structural materials experience, diffuse and begin to cluster together, forming a sink for other vacancies. These clusters form voids and then microcracks, which undermine the mechanical strength of the structural material. However, if vacancy diffusion in the structural material were slowed or stopped, the formation of voids and microcracks could be avoided and material mechanical strength preserved. The vacancy migration energy barrier (VMEB) plays a key role in determining the diffusion rate of these vacancies, and is exponentially inversely proportional to their hopping rate (diffusing from one atomic site to another) according to Einstein's diffusion equation [7]. Thus, increasing the vacancy migration energy barrier can maintain the mechanical strength of nuclear structural materials. One common method to change VMEB is alloying, thus we consider an existing alloy: stainless steel-316 (SS-316).

The SS-316 alloys have a history as nuclear structural materials (80 years in the case of SS-316H) [8], and at least one alloy (SS-316H) has been considered for generation IV reactors (molten salt, sodium-cooled fast, lead-cooled fast, and super critical water reactors) [9]. It is also one of the only alloys the American Society of Mechanical Engineers has qualified for high temperature applications in nuclear reactors [10]. However, the sensitivity of VMEB on vacancy nearest neighbor is not understood, which may be critical to understanding which compositions offer the highest VMEB, and therefore, best irradiation damage resistance. Unfortunately, this is difficult to explore experimentally due to, among other reasons, the length scale, speed, and temperature at which these vacancies diffuse. Thus, we apply density functional theory (DFT) in combination with an Ising model and the machine learned nudged elastic band (MLNEB) method to calculate VMEB for SS-316. As an initial case, and for comparison, we also calculate VMEB for face-centered cubic (FCC) Fe.

In this work, we apply DFT in combination with MLNEB to calculate VMEB for SS-316 and FCC Fe. FCC Fe is included because it shares the FCC crystal structure, bulk paramagnetism at temperatures of interest [1, 11], and the majority of its composition with SS-316. We note that paramagnetism is often modeled by non-magnetic (NM) calcualtions, and that there is some experimental confirmation for bulk NM behavior [12]. An Ising model is applied in order to include finite temperature effects in both systems and justify 0 K calculation results at finite temperature. We predict that vacancy presence in FCC Fe induces a local ferromagnetic domain, and increases the net magnetic moment of SS-316 by 3.7 μ_B (the antiferromagnetic ordering of SS-316 is maintained). While vacancy induced local magnetic changes have been documented in BCC Fe [13], the same has not been reported for FCC Fe. We further predict that inclusion of a vacancy either in FCC Fe or SS-316 increases the paramagnetic transition temperature of the material. Finally, we predict a low VMEB for FCC Fe (0.25 eV) and higher, though varied VMEB in SS-316, which are sensitive to the element diffusing opposite the vacancy (0.65, 0.82, and 1.2 eV for Cr, Fe, and Ni, respectively).

1.2 MATHEW'S INTRO

The quantitative irradiation-driven microstructure evolution prediction requires accurate predictions of the number of remaining point defects generated by irradiation damage cascades after their initial recombination. Two different metrics to model defect recombination include the recombination radius and spontaneous recombination distance [14, 15]. There is an underlying assumption that defect recombination is the same in the two processes used to model defect recombination and that the same metrics can be used to measure and describe them (e.g., the distance that defects must be separated to avoid recombination). However, the pros and cons of each of these methods have not previously been directly compared.

In this work, we used molecular dynamics simulations of collision cascades to investigate how different materials respond to radiation induced damage, which provides a test bed to compare both defect recombination models over a variety of material systems. This comparison also provides additional valuable insight about the collision cascade and recombination that takes place after the thermal spike phase of the collision cascade. Five different materials with a combination of face-centered cubic (fcc) and body-centered cubic (bcc) metals were investigated in order to capture the defect dynamics and microstructural evolution of metals with a variety of different material properties. The metals studied in this work are nickel (Ni), aluminum (Al), copper (Cu), iron (Fe), and molybdenum (Mo). A detailed profile of the time evolution of a collision cascade was calculated for each material at a range of initial energies. The effect of the initial energy and material properties on the maximum extent of the cascade damage was investigated, and both the recombination distance and recombination radius of the point defects during the recombination process were calculated.

2. Machine Learning and Density Functional Theory

2.1 Methods

2.1.1 Density Functional Theory

DFT is a quantum mechanics-based method that allows for solutions to Schrodinger's equation [16], defined as:

$$\hat{H}\Psi = E\Psi \tag{1}$$

where $\hat{H}$ is the Hamiltonian that operates on Ψ, Ψ is the wavefunction, and E is the energy of the system. Applying the Born-Oppenheimer approximation, which assumes that the electronic and nucleic wavefunctions can be treated separately due to mass differences (treating the nuclei as spatially static relative to the electrons), Eqn. 1, as applied to the electronic energy of the system, can be expanded to:

$$\left[\sum_{i=1}^{N}(-\frac{\hbar}{2m_i}\nabla_i^2) + \sum_{i=1}^{N} V(\boldsymbol{r}_i) + \sum_{i<j}^{N} U(\boldsymbol{r}_i, \boldsymbol{r}_j)\right]\Psi = E\Psi \tag{2}$$

where $\hbar$ is the reduced Planck's constant, m_i is the mass of the ith electron, V refers to the potential energy originating from the atomic nuclei, $\boldsymbol{r}$ is the position vector, and U is the potential energy originating from the electron-electron interaction. DFT arises from two results by Hohenberg and Kohn in 1964 [17]: (i) the electron density can be used by functionals to describe the external potential felt by electrons ($V(\boldsymbol{r})$) and (ii) the ground state energy (E_{gs}) is a minimum bound, given the electron density is exact. Kohn and Sham [18] later developed equations based on the time-independent Schrodinger equation [16] allowing for external potential calculation. These equations allow DFT to be a viable computational method for modeling materials. Because the equations developed by Kohn and Sham are time-independent and E_gs occurs at 0 K by definition, DFT calculations deal with static systems at 0 K. Electronic wavefunctions are commonly expanded to one of many basis sets, which, in solid state calculations, is often the plane wave basis set. A mesh of reciprocal space points is used to take advantage of the crystallinity inherent in many solid systems. Given that E_gs is a minimum bound for a given structure's energy, coefficients associated with the chosen basis set are adjusted iteratively until convergence criteria (usually minimum energy or force values) are. This process affords DFT considerable accuracy, though with expensive computational cost, usually limiting calculations to 1000 atoms.

All quantum mechanical properties were calculated using DFT in the Vienna Ab-initio Simulation Package (VASP) [19, 20] within the periodic boundary condition approach. The Perdew-Burke-Ernzerhof (PBE) form of the generalized gradient approximation (GGA) exchange-correlation functional [21] with the projector augmented wave (PAW) pseudopotentials [22] were employed. No Hubbard correction was used due to the metallic nature of the systems investigated. Typically PM systems such as FCC Fe and SS-316 have been modeled by non-collinear or NM calculations [23], though FM and AFM have also been applied [24]. However,

non-collinear calculations did not maintain a cubic structure, so NM calculations were performed, along with FM (or spin polarized) calculations for comparison for FCC Fe. AFM calculations are omitted because FM calculations have been shown to differ in vacancy formation energy by only 0.02 eV [24]. Spin polarized (or FM) calculations allowed spins to relax. DFT calculations used a summation of plane waves with energies up to 650 eV for FCC Fe (32 atom system) and 600 eV for SS-316 (54 atom system). Increasing the cutoff value to 700 and 650 eV altered system energies by only 6.3×10^{-3} and 7.6×10^{-3} eV, respectively. Gamma point centered k-point meshes of 12x12x12 and 4x4x4 were chosen for the FCC Fe and SS-316 systems, respectively, because increasing these meshes to 14x14x14 6x6x6 only altered the system energies by 1.1×10^{-3} and 8.8×10^{-3} eV. First order Methfessel-Paxton smearing of the bands were applied with a width of 0.10 eV. The electronic convergence criterion was set to 1.0×10^{-5} eV for all DFT calculations. Geometries were optimized until they converged to energy changes of less than 1.0×10^{-4} eV. We note that vacancy concentration in FCC Fe and SS-316 is very high (0.2 at. %). However, the vacancy concentration in FCC Fe is decreased (to 2.5×10^{-4} at. %), the predicted magnetic transition temperature is the same. Thus, we consider our vacancy concentration value reasonable for magnetic transition temperature prediction.

The stochastic nature of the solid solution SS-316 material was accounted for through application of special quasirandom structures [25]. This is accomplished by generating a large number of structures and comparing the radial distribution functions of each until a sufficiently close match to the targeted random substitution is found. Our SQS generated SS-316 resulted in an MAE of 1.2×10^{-3} or 1.1 %. The SS-316 composition in this work omits minor compounds and uses a composition of 66 at. % Fe, 22 at. % Cr, and 11 at. % Ni.

2.1.2 Machine Learned Nudged Elastic Band

Machine learned nudged elastic band (ML-NEB) builds on the well-established nudged elastic band (NEB) method to learn the potential energy surface (PES) and activation energy barrier of a given material. We first briefly review the NEB method, and then review the ML-NEB method.

The NEB method finds the saddle point and minimum energy path between a reactant-product pair. This is accomplished by relaxing a series of interpolated atomic configurations, known as images, along the reaction pathway while maintaining equal space between each image. This spacing is maintained through spring forces applied along the band. These spring forces also project a force component against the slope of the PES perpendicular to the band so that the band is nudged towards the saddle point (or transition state) of the PES between the reactant and product [26].

The ML-NEB method builds on the NEB method by application of Gaussian process regression (GPR). Images are generated as in the NEB method, but they are relaxed electronically instead of ionically. The potential energy surface is then regressed by GPR, and those images whose force uncertainty (obtained from the GPR fit) is above a predetermined convergence criteria, are relaxed ionically. This process continues until the convergence criteria, usually force uncertainty, is met

[27, 28]. We bench marked the MLNEB method against traditional NEB, and found MLNEB completed 2.3 times faster and differed from NEB calculated migration energy barrier by only 2.7×10^{-2} (1.0 %) for FCC Fe. SS-316 MLNEB calculations converged in under 48 hours; however, because NEB calculations did converge within a month, no comparison was made.

2.1.3 Ising Model

The Ising model allows for application of DFT information to predict magnetic transition temperatures. Because DFT calculations occur at 0 K (excepting ab initio molecular dynamics), temperature effects, and by extension, calculation of magnetic transition temperatures, are not possible. However, DFT can approximate the energy required to flip a spin a system, which the Ising model can use to account for temperature effects. The Ising model uses statistical mechanics to model ferromagnetism. This model constructs a periodically bounded lattice and assigns each site a spin value of either +1 or -1 (thus Ising model results are not to be taken as actual spin values, rather and indication of the magnetic structure). Neighboring sites interact: those with like spin have lower energy than those with unlike spin. Though the system tends towards the lowest energy configuration, temperature disrupts this, and so the magnetic structure can change with changes in temperature [29].

Python code [30] available on Github that applied the Ising model on a 2-dimensional square lattice was extended to a 3-dimensional face centered cubic lattice. A Metropolis algorithm was used to apply the DFT calculated J term to the Ising model [31] using Monte Carlo moves. A 5x5x5 supercell was used, with a total of 62 atomic sites for both FCC Fe and SS-316.

Magnetic interaction terms (J) were approximated by linearly fitting the change in system energy as a function of magnetic spin-flip. The relationship between energy and spin-flip was established by enforcing different net magnetic moments on a given system and calculating their respective energies by DFT. The J term was then determined by multiplying the resulting slope by two to account for spin-flip effects on the net magnetic moment.

2.2 Results

2.2.1 Face Centered Cubic Iron

This section will first discuss determining the local magnetic structure of FCC Fe containing a vacancy by application of DFT and the Ising model, followed by the prediction of the VMEB of this material by MLNEB.

Ferromagnetic (FM) initialized DFT calculations are shown to be appropriate for vacancy modeling in FCC Fe and imply vacancies induce local ferromagnetism. Calculations initialized with FM ordering showed lower energy than NM calculations, both in the pristine case (difference of 0.19 eV) and more so in the vacancy case (difference of 0.93 eV). Additionally, FM calculations agree with experimental lattice constant measurements [32] better than NM calculations (errors of 0.01 Å or 0.39 % and 0.20 Å or 5.5 %, respectively). Finally, in agreement with previous work [24],

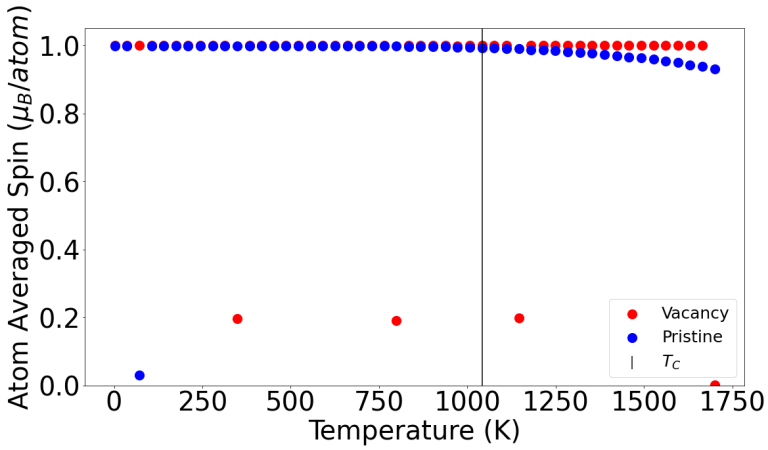

Figure 1: Ising model results for FCC Fe. The T_C of pristine FCC Fe [1] is approximated and ferromagnetism is predicted well beyond this temperature when a vacancy is present.

FM calculations approximate experimental vacancy formation energy well (error of 1.2×10^{-2} eV or 0.68 %) [33], as found by [24]. This agreement with experiment shows FM initialized DFT calculations are appropriate for FCC Fe, especially in the presence of a vacancy. Further, the increased energy difference from the pristine to vacancy system implies that the vacancy may induce a local FM domain in FCC Fe. To validate these implications at finite temperature the Ising model is applied.

Application of the Ising model confirms vacancies induce local FM domains in FCC Fe (see Fig. 1). Extending these DFT results to finite temperatures, the Ising model approximates the Curie Temperature (T_C) of FCC Fe [1]. In the presence of a vacancy, T_C approaches the melting point (1811 K) [34] of FCC Fe. Therefore, we predict the FM ordering is appropriate for FCC Fe. Now that the correct local magnetic domain has been determined, the migration energy barrier can be calculated.

MLNEB predicts a low VMEB (0.25 eV) for FCC Fe (see Fig. 2), implying that pure FCC Fe has poor radiation resistance. Interestingly, this FM calculated VMEB is over five times lower that NM calculations. However, VMEBs can be increased through alloying, improving radiation resistance. We therefore calculate the magnetic structure and VMEB for an Fe alloy: SS-316.

2.2.2 Stainless Steel 316

Ferromagnetic (FM) initialized DFT calculations are shown to be appropriate for vacancy modeling in FCC Fe and imply a vacancy-induced increase in the magnetic transition temperature, or Néel temperature (T_N). Calculations initialized with FM ordering again showed lower energy than NM calculations, both in the pristine case (difference of 2.5 eV) and in the vacancy case (difference of 3.0 eV). We note that despite a FM initialization, the spin of the Cr atoms show antiferromagnetic (AFM) alignment with respect to those of the Fe and Ni atoms, in agreement with previous work [35, 36]. We also note that the net magnetic moment increased by 3.7 μ_B,

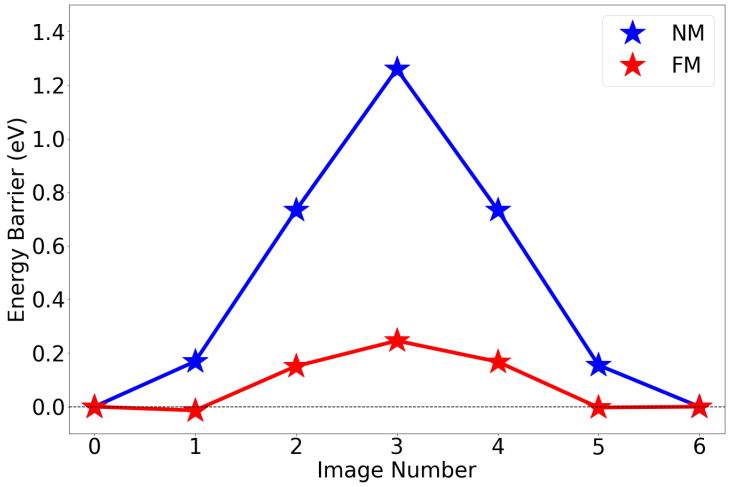

Figure 2: Energy pathway for vacancy diffusion in FCC Fe, showing both FM and NM cases. Image number refers to the images or spatial configuration of the atoms as the vacancy diffuses from one site to another.

generally becoming more FM. The FM initialized lattice constant also shows better agreement with experiment [37] as compared to NM calculations (error of 0.05 Å or 1.4 % and 0.11 Å or 3.2 %, respectively). Finally, FM initialized calculations agree well with previous DFT work for Cr vacancy formation energies (error of 3.1×10^{-2} eV or 1.2 %) [38]. As with FCC Fe, this agreement of FM initialized DFT calculations imply these calculations are appropriate for SS-316, especially in the presence of a vacancy. Magnetically, the vacancy case increases spin per atom by 0.11 μ_B or 11 % relative to the pristine case. This implies a stronger locally ordered spin domain and should result in an increase in T_N. However, finite temperature effects, such as applied by the Ising model, are required to verify this prediction.

Application of the Ising model further supports a vacancy induced increase in T_N (see Fig. 3). Because the Ising model assumes the system is at some temperature FM, there are discrepancies with our DFT work, previous DFT work [35, 36], and experiment [11]. Instead of an AFM structure at low temperatures (¡ 25 K), the Ising model predicts SS-316 to be FM, and consequently, the Ising does not approximate T_N well for SS-316. Despite these disagreements, the is a clear shift in the calculated magnetic transition temperature when a vacancy is present shows the vacancy's impact on local magnetism in SS-316. This is further supported given the fact that the SS-316 system, though AFM, is mostly FM (76 % by composition, 82 % by spin), and so the FM assumptions in the Ising model should approximate AFM to PM transition temperatures. Now that the correct local magnetic domain has been determined, the migration energy barrier can be calculated.

MLNEB predicts VMEBs in qualitative agreement with experiment [39] (see Fig. 4). Specifically, for atoms diffusing opposite the vacancy, Cr has to the lowest barrier, followed by Fe, and then by Ni (values of 0.65, 0.82, and 1.2 eV, respectively). These results imply slower vacancy diffusion in SS-316 relative to FCC Fe. Further, the differences in energies at image 6 in Fig. 4 imply that vacancy nearest neighbor configuration will affect VMEB values. However,

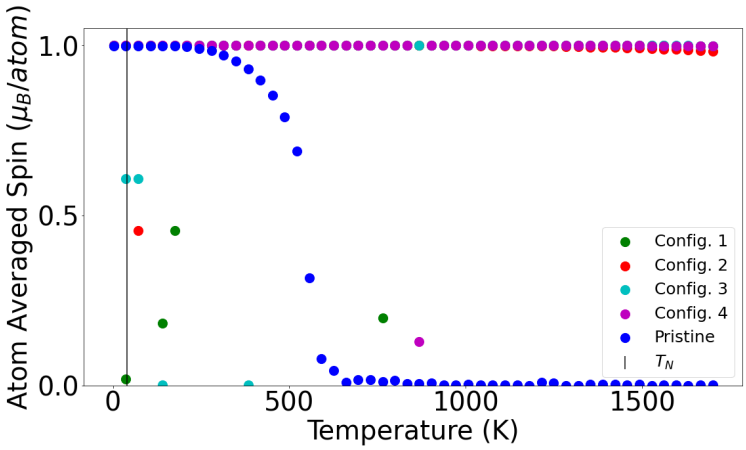

Figure 3: Ising model results for SS-316. Ferromagnetism is predicted well beyond this temperature when a vacancy is present, regardless vacancy's nearest neighbors.

more MLNEB calculations are required to understand the effects vacancy nearest neighbors on VMEBs in SS-316. Once completed, these results can be applied to a kinetic Monte-Carlo model, allowing for prediction of vacancy diffusion rates.

2.3 Impact

3. Molecular Dynamics of Collision Cascades in Metals

3.1 Methods

Molecular dynamics is a technique for modeling the behavior of a system consisting of an ensemble of atomic particles using the classical Newtonian equations of motion. The motion of each atom in the simulation is tracked through time by determining the forces acting upon it using an interatomic potential and then numerically integrating in time to obtain its position at the next time step of the simulation. In this work the MD simulations were performed using LAMMPS (large scale atomistic/molecular massively parallel simulator), an open source package developed by Sandia National Laboratories [40] that is highly optimized for running MD simulations across many CPU cores and/or GPUs. Modeling the high energy collisions involved in collision cascades, these simulations need to account for the forces arising from a variety of physical phenomena, requiring the combination of several models to accurately represent the forces in the system.

3.1.1 Molecular Dynamics Models

The forces between two interacting particles is considered to be the most fundamental aspect of radiation damage, without which it is impossible to define microstructural properties and defect energetics. These interatomic potentials are typically empirical functions created from fitting either density functional theory or experimental data, and their accuracy is vital for the accuracy

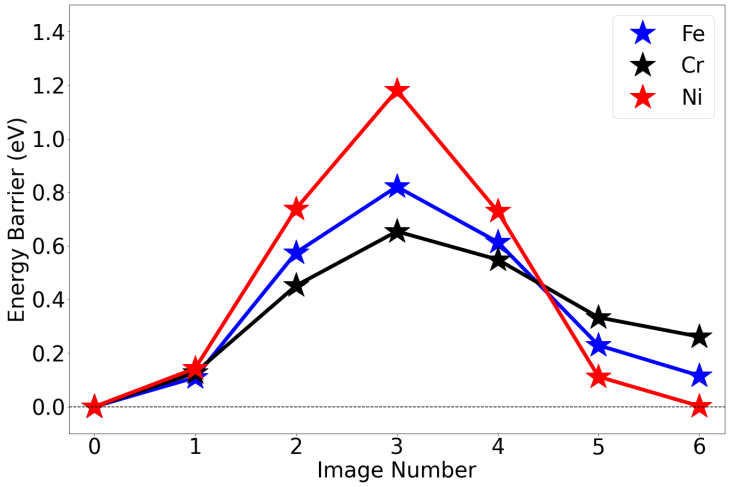

Figure 4: Energy pathway for vacancy diffusion in SS-316. Legend shows the species which diffuses opposite the vacancy. Image number refers to the images or spatial configuration of the atoms as the vacancy diffuses from one site to another.

of simulation outcomes. The forces modeled in this work can be broken down into three separate components. The first is long range forces, which we are modeling using potentials based on the Embedded Atom Method (EAM) [41]. In this work, the Embedded Atom Model (EAM) potentials developed by Mendelev et al. [42], Bonny et al. [43], Mendelev et al. [44], Mishin et al. [45], and Ackland et al. [46] are used to define the interactions of Al, Ni, Fe, Cu, and Mo, respectively, for the collision cascade simulations. Short range forces resulting from screened nuclear repulsion are modeled using the Ziegler, Biersack and Littmark (ZBL) potential [47]. The ZBL was phased in for closely spaced atoms starting at 1.4 A and increasing to full strength at 1.0 A. The last component is an electronic stopping model that accounts for the inelastic energy loss of fast moving atoms in solids due to electronic collisions [48, 49]. The strength of the electronic stopping power in each material was calculated using the Stopping and Range of Ions in Matter program (SRIM) [47].

3.1.2 Collision Cascade Simulations

In order to model the development of a collision cascade and subsequent recombination process we first start with a large simulation box with periodic boundary conditions. A simulation with a supercell size of 70x70x70 unit cells was found to be sufficient to contain all of the displaced atoms within the computational domain, avoiding the spurious effects of cascade self-interaction with periodic boundary conditions. The typical lattice for each metal type was then generated in the simulation box, and the simulation was then equilibrated for 50 ps at temperature of 300 K and 1 bar using a Nosé–Hoover thermostat and barostat [50, 51].

The collision cascade simulations are then performed using primary knock-on atoms (PKA) with a range of initial energies between 1 keV and 15 keV, with an additional set of simulations for Mo at 20 keV. The displacement cascades were initiated by choosing a random atom near the center of the computational domain as the PKA. The PKA was then assigned a velocity

corresponding to the desired initial PKA energy in a random direction. To capture the cascade propagation with the correct dynamics, the time step size is adjusted at different stages of the cascade propagation. During the ballistic phase, a time step of 0.01 fs is used to simulate the collision cascade for the first 1.5 ps of the cascade. As the kinetic energy of displaced atoms is transferred to other atoms and dissipated in the system, the velocity of the displaced atoms decreases, and the time step is increased to 0.1 fs until 6.5 ps, and finally the time step is increased to 1 fs for the rest of the simulation. The cascade simulations are run to 36.5 ps to achieve a steady state in the number of remaining defects. It should be noted that the cascades generated in this work produce most of the basic physical phenomena of primary radiation damage. To remove the bias of the initial PKA direction on the collision cascades simulations, the simulations were repeated using 10 random directions for each metal and PKA energy.

In order to remove the excess heat produced from the gradual dissipation of the applied kinetic energy, a Nosé–Hoover thermostat is applied far away from the collision cascade. This thermostat is used to keep atoms within 1 unit cell of the edges of the simulation domain at a temperature of 300 K. At the end of the simulation, the average temperature of the entire system has returned to the initial value. The identification of defects, including visualization, quantification, and categorization, is carried out using the Wigner-Seitz method [49], which is implemented both in LAMMPS and with the visualization tool OVITO [52]. The Wigner-Seitz method compares the crystal structure of the irradiated material system with a non-irradiated equilibrated material as the reference structure. The number and location of defects is calculated every 1000 time steps.

3.2 Results

Collision cascade simulations quantify the recombination after the thermal spike phase, allowing us to study the production and annihilation of defects at different stages of the displacement damage cascade. Figure 5 shows the production and annihilation of the defects at different steps of the displacement cascade for all five metals. As can be observed from the time evolution of the cascade, the maximum size of the cascade has a non-linear relationship with the initial PKA energy. Additionally the choice of metal also plays a significant role in the size of size of the cascade, with higher mass elements generally corresponding to a smaller cascade size for a given PKA energy.

After the cascade has reached its peak size between 0.2 ps and 1.2 ps, the number of defects begins to decreasing due to the recombination of interstitial atoms and vacant sites. Eventually the defect concentration reaches a quasi-steady-state concentration for times approximately ≥ 10 ps. The PKA simulations are carried out up to 36.5 ps to confirm the quasi-steady-state defect concentration. At the end of each cascade simulation, we observed a homogeneous temperature. Regardless of the initial PKA direction, no radiation-induced amorphization is observed in the cascade structure, which is in agreement with other MD simulations.

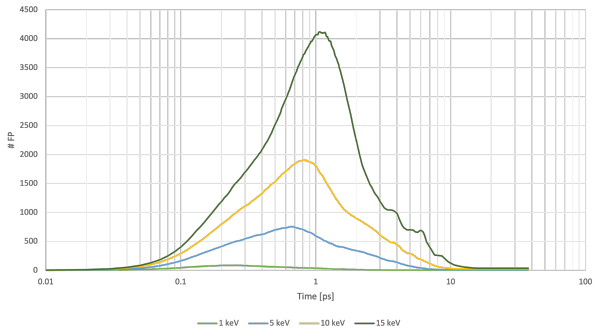

(a) Al

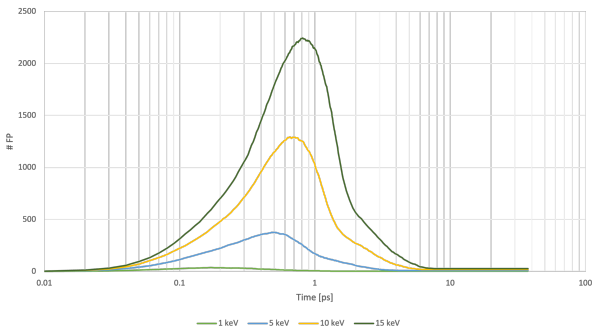

(b) Ni

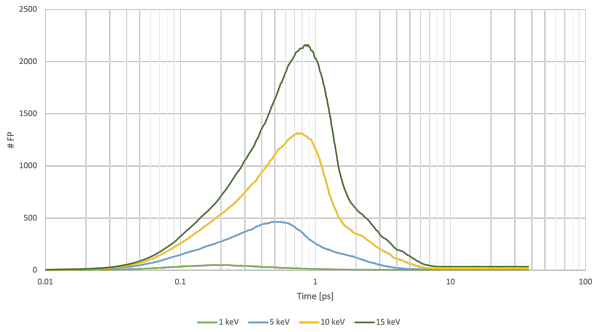

(c) Fe

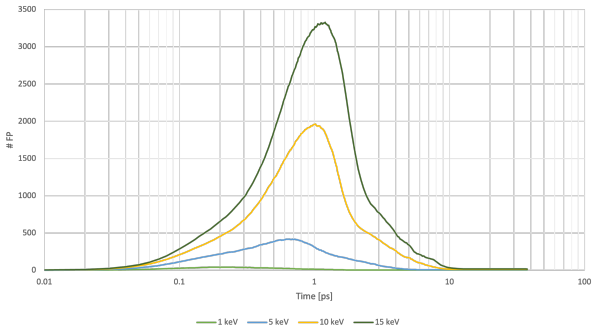

(d) Cu

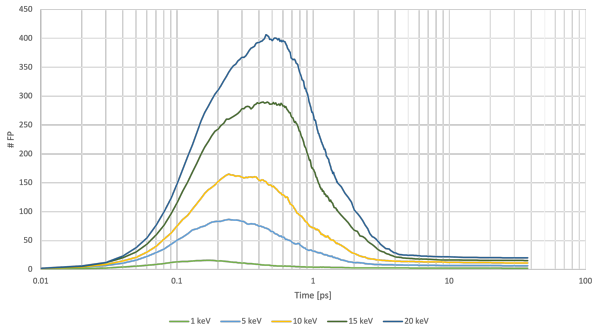

(e) Mo

Figure 5: The average time evolution of cascade-created Frenkel pairs in Al, Ni, Fe, Cu, and Mo. Each profile shown is the average of 10 simulations.

Material System	c [m/s]
Al	6420
Ni	6040
Fe	5950
Cu	4760
Mo	6250

Table 1: Experimental longitudinal speed of sound values at 293 K and 1 Atm of pressure from *CRC Handbook of Chemistry and Physics* [53].

3.2.1 Peak Cascade Damage

Specifically looking at early development of the cascade, it is clear that an PKA energy will on average result in an increase in the maximum number of defects generated. However, this relationship only holds for collision cascades in the same material. In order to better explain the physical phenomena governing how large a collision cascade grows for a given amount of initial energy, we need to identify a relation that can predict the maximum size that the cascade can grow as a function of the initial energy and the material properties.

A particularly useful quantity for analyzing the interaction of fast and slow moving particles is the Mach Number (Ma). This dimensionless quantity essentially describes the ratio between how fast the PKA atom is moving to the speed at which the rest of the medium can react to the PKA's presence. Where the Mach Number can be calculated as:

$$\mathrm{Ma} = \frac{v}{c} \tag{3}$$

where v is the initial PKA velocity and c is the speed of sound in the material. For this analysis we will be using previously published experimental values for the longitudinal speed of sound located in Table 1.

As shown in Figure 6, We find that there is a strong correlation between the initial Mach Number for a PKA and peak number of vacancies created in a given cascade. The optimal fit for the average number of peak vacancies was found to be

$$N_v = 0.0325\,\mathrm{Ma}^3, \tag{4}$$

with an R^2 value of 0.93. This is quite interesting because it means that the initial Mach Number of the PKA can explain the vast majority of the difference in peak cascade size. Additionally this provides a convenient method for estimating the maximum cascade size using just the PKA energy and experimental material properties, prior to running any atomistic simulations.

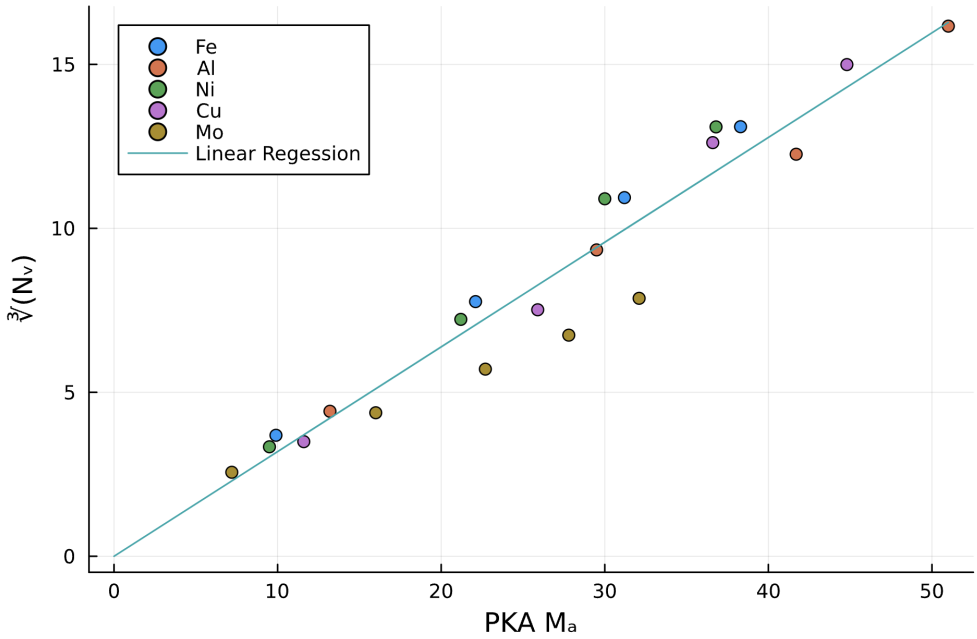

Figure 6: Relation between maximum cascade size and the initial mach number of the PKA. Linear regression shown has $R^2 = 0.93$

3.2.2 Recombination and Spontaneous Recombination Distance

After the collision cascade has reached its peak size, we enter the recombination phase which is dominated by the recombination of vacancies and interstitials. This phase is governed by defect morphology and the diffusion of vacancies and interstitials over short timescales. More specifically we want to look at the Spontaneous Recombination Distance (SRD), from the irradiation damage cascade simulations, as well as direct measurement of the final minimum recombination radius (Rr). The meanings of SRD and R_r are schematically represented in Figure 7. The spontaneous recombination distance is defined as the physical separation distance of the interstitial and vacancy of a Frenkel pair needed to survive immediate recombination. In practice, this is the distance between the outer edge of the vacancy core and the inner edge of the interstitial shell that forms from a collision cascade [15]. Conversely, the recombination radius treats the vacancy as a spherical sink with a radius, R_r, that will capture and recombine with a diffusing interstitial [14].

During the collision cascade, the kinetic energy of the incident neutron or ion is transferred to the target material. Ideally for small PKA energies, the interstitial and vacancy zones are considered spherical; however, in reality, the interstitial and vacancy contours have different shapes. From this data, the difference between the contours can be identified and the approximate distance between most of the vacancies and interstitials can be identified. The vacancies and interstitials within the recombination radius are annihilated, leaving behind a perfect lattice. Only a few defects remain, namely those which are sufficiently far apart, with the distance between

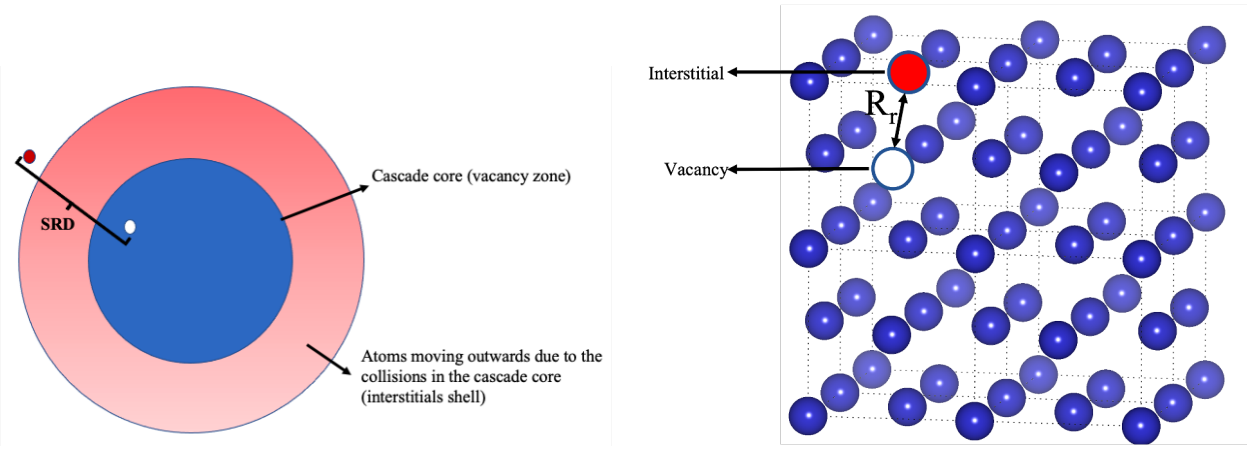

(a) (b)

Figure 7: A schematic representation of the SRD and the recombination radius (R_r). White circles represent individual vacancies and red circles represent individual interstitials. (a) The spontaneous recombination distance in a collision cascade. The blue region represents the cascade core, which is rich in vacancies, and the red region represents the region rich in displaced atoms that forms an interstitial shell. (b) The recombination radius is calculated by treating the vacancy as a spherical sink with a radius, R_r, that will capture and recombine with a diffusing interstitial and result in a perfect crystal lattice. The distance between the interstitial and vacancy is referred to as the recombination radius.

them being greater than the spontaneous recombination distance.

To extract this data from our collision cascade simulations we measured the the contours of the interstitial shells and vacancy cores using OVITO. Additionally, we also recorded the average minimum recombination distance from our simulations during the relaxation phase in order to allow for a comparison of these two methods. The results of this analysis are presented in Table 2.

The results indicate that both methods produce similar values for SRD and R_r, which are within the error bounds on our measurements. It evident from our results that there are pros and cons to each method. When calculating the SRD, we rely heavily on the assumption that the cascade damage is spherical. However, this assumption appears to start breaking down as the PKA energy increases. For a PKA energy of 1 keV we find that our SRD measurment has a relative error of 38%, but the relative error increases to 76% at a PKA energy of 5 keV. On the other hand the relative error for the R_r measurements were much more consistent, with relative errors between 15% and 19% for all tested PKA energies. However this method did have issues in a few specific simulations with very low PKA energies, resulting from there being very few vacancies or interstitials.

4. CONCLUSIONS

[Please write individual section conclusions and Andrea can massage them together.]

Material System	PKA Energy [eV]	Average Radius of Vacancy Zone [A]	Average Radius of Interstitial Zone [A]	SRD [A]	R_r [A]
Fe	1000	8.5	12.4	3.9	6.5
Fe	5000	13.5	19.3	5.8	8.5
Fe	10000	22.3	28.0	5.7	6.1
Fe	15000	36.2	42.3	6.1	6.4
Al	1000	13.9	17.9	3.9	11.2
Al	5000	28.2	33.4	5.2	9.7
Al	10000	39.7	44.6	4.9	7.4
Al	15000	50.9	57.0	6.0	7.1
Ni	1000	7.2	10.5	3.3	8.7
Ni	5000	13.1	17.7	4.6	5.7
Ni	10000	17.5	23.8	6.3	6.9
Ni	15000	25.8	33.1	7.3	4.8
Cu	1000	8.0	12.2	4.3	9.8
Cu	5000	15.1	19.7	4.5	10.6
Cu	10000	22.6	28.5	5.9	9.4
Cu	15000	32.2	38.3	6.1	8.9
Mo	1000	7.4	11.6	4.1	13.2
Mo	5000	15.3	19.9	4.6	8.8
Mo	10000	33.3	37.8	4.5	8.4
Mo	15000	25.1	30.2	5.1	6.4
Mo	20000	28.3	32.7	4.4	6.8

Table 2: Quantification of the average spontaneous recombination distance (SRD) and recombination radius (R_r) obtained from the collision cascade simulations.

4.1 TANNERS CONCLUSION

FCC Fe and SS-316 have been studied through application of DFT, an Ising model, and MLNEB. The DFT prediction of local FM and AFM domains in otherwise PM FCC Fe and SS-316, respectively, and their confirmation by the Ising model at finite temperature, has mechanical strength issues. These local magnetic domains can affect the phase [54–56], and thus mechanical strength of metallic systems, making vacancies even more critical to mechanical failure. Further, this implies magnetization of these materials could have a more significant impact on their mechanical strength than other metallic systems. MLNEB predicted VMEB for FCC Fe further shows the importance of magnetism, as the calculated FM VMEB is over five times smaller than that of the NM case, which magnetic ordering has been measured by some to be the bulk ordering [12]. MLNEB predicted VMEB for SS-316 show that both element diffusing opposite the vacancy and the composition of vacancy's nearest neighbors. In summary, this work shows the impact defects can have on local magnetic structure in materials, and how they can affect the migration of these defects, thus affecting the mechanical strength of these materials.

4.2 MATHEWS CONCLUSION

Molecular dynamics simulations of collision cascades have been used to study the behavior of Frenkel defects in a variety of pure materials. The development of the cascade was profiled using the Wigner-Seitz method to determine how the peak size of the collision cascade was influenced by the choice of material. The size of the cascade was found to be strongly correlated with the initial Mach number of the PKA, which suggests that properties related to the speed of sound (such as bulk modulus and thermal conductivity) may influence the average number of initial number of point defects created during a collision cascade.

Additional analysis of the collision cascade simulations was performed to investigate the recombination of point defects during the recombination phase of the cascade. The distance at which vacancies and interstitials recombine was calculated using two methods, spontaneous recombination distance and recombination radius. Both methods produced similar values; however the recombination radius method resulted in significantly less variance while also working well at higher PKA energies. As such calculating the recombination radius should be the preferred method going forward.

REFERENCES

[1] C. Kittel, Introduction to solid state physics, John Wiley & sons, inc, 1986.

[2] K. R. Voorspools, E. A. Brouwers, W. D D'haeseleer, Energy content and indirect greenhouse gas emissions embedded in 'emission-free'power plants: results for the low countries, Applied Energy 67 (3) (2000) 307–330.

[3] T. Todd, R. Wigeland, Advanced separation technologies for processing spent nuclear fuel and the potential benefits to a geologic repository, in: Separations for the Nuclear Fuel Cycle in the 21st Century, ACS Publications, 2006, pp. 41–55.

[4] K. L. Nash, G. J. Lumetta, S. B. Clark, J. Friese, Significance of the nuclear fuel cycle in the 21st century, in: Separations for the Nuclear Fuel Cycle in the 21st Century, ACS Publications, 2006, pp. 3–20.

[5] D. J. Rose, Nuclear eclectic power, Science 184 (4134) (1974) 351–359.

[6] I. Pioro, Handbook of generation IV nuclear reactors, Woodhead Publishing, 2016.

[7] A. Einstein, Zur theorie der brownschen bewegung, Annalen der Physik 19 (1906) 371–381.

[8] W. Ren, L. Lin, Consideration of thermal embrittlement in alloy 316h for advanced non-light water reactor applications, in: Pressure Vessels and Piping Conference, Vol. 58981, American Society of Mechanical Engineers, 2019, p. V06BT06A016.

[9] T. Allen, F. Balbaud-Celerier, T. Asayama, M. Pouchon, J. Busby, S. Maloy, J. Park, C. Fazio, Y. Dai, P. Agostini, et al., Status report on structural materials for advanced nuclear systems, Tech. rep., Organisation for Economic Co-Operation and Development (2013).

[10] Asme boiler and pressure vessel code, section iii rules for construction of nuclear facility components, division 5 high temperature reactors (2017).

[11] L. D. Flansburg, N. Hershkowitz, Magnetism in austenitic stainless steels, Journal of Applied Physics 41 (10) (1970) 4082–4086.

[12] R. Reed-Hill, R. Abbaschian, Dislocations and plastic deformation, Physical Metallurgy Principles (1994) 124–167.

[13] H. Wen, P.-W. Ma, C. Woo, Spin-lattice dynamics study of vacancy formation and migration in ferromagnetic bcc iron, Journal of nuclear materials 440 (1-3) (2013) 428–434.

[14] K. Nordlund, S. J. Zinkle, A. E. Sand, F. Granberg, R. S. Averback, R. E. Stoller, T. Suzudo, L. Malerba, F. Banhart, W. J. Weber, F. Willaime, S. L. Dudarev, D. Simeone, Primary radiation damage: A review of current understanding and models, Journal of Nuclear Materials 512 (2018) 450–479. doi:https://doi.org/10.1016/j.jnucmat.2018.10.027.
URL https://www.sciencedirect.com/science/article/pii/S002231151831016X

[15] K. Nordlund, S. J. Zinkle, A. E. Sand, F. Granberg, R. S. Averback, R. Stoller, T. Suzudo, L. Malerba, F. Banhart, W. J. Weber, F. Willaime, S. L. Dudarev, D. Simeone, Improving atomic displacement and replacement calculations with physically realistic damage models, Nature Communications 9 (1) (2018) 1084. doi:10.1038/s41467-018-03415-5.
URL https://doi.org/10.1038/s41467-018-03415-5

[16] E. Schrödinger, An undulatory theory of the mechanics of atoms and molecules, Physical review 28 (6) (1926) 1049.

[17] P. Hohenberg, W. Kohn, Inhomogeneous electron gas, Physical review 136 (3B) (1964) B864.

[18] W. Kohn, L. J. Sham, Self-consistent equations including exchange and correlation effects, Physical review 140 (4A) (1965) A1133.

[19] G. Kresse, J. Furthmüller, Efficient iterative schemes for ab initio total-energy calculations using a plane-wave basis set, Physical review B 54 (16) (1996) 11169.

[20] G. Kresse, J. Furthmüller, Efficiency of ab-initio total energy calculations for metals and semiconductors using a plane-wave basis set, Computational materials science 6 (1) (1996) 15–50.

[21] J. P. Perdew, K. Burke, M. Ernzerhof, Generalized gradient approximation made simple, Physical review letters 77 (18) (1996) 3865.

[22] G. Kresse, D. Joubert, From ultrasoft pseudopotentials to the projector augmented-wave method, Physical review b 59 (3) (1999) 1758.

[23] H. Wang, X. Gao, H. Ren, S. Chen, Z. Yao, Diffusion coefficients of rare earth elements in fcc fe: A first-principles study, Journal of Physics and Chemistry of Solids 112 (2018) 153–157.

[24] K. Li, C.-C. Fu, A. Schneider, Effects of magnetic excitations and transitions on vacancy formation: cases of fcc fe and ni compared to bcc fe, Physical Review B 104 (10) (2021) 104406.

[25] A. Zunger, S.-H. Wei, L. Ferreira, J. E. Bernard, Special quasirandom structures, Physical review letters 65 (3) (1990) 353.

[26] H. Jónsson, G. Mills, K. W. Jacobsen, Nudged elastic band method for finding minimum energy paths of transitions, in: Classical and quantum dynamics in condensed phase simulations, World Scientific, 1998, pp. 385–404.

[27] M. H. Hansen, J. A. G. Torres, P. C. Jennings, Z. Wang, J. R. Boes, O. G. Mamun, T. Bligaard, An atomistic machine learning package for surface science and catalysis, arXiv preprint arXiv:1904.00904.

[28] J. A. G. Torres, P. C. Jennings, M. H. Hansen, J. R. Boes, T. Bligaard, Low-scaling algorithm for nudged elastic band calculations using a surrogate machine learning model, Physical review letters 122 (15) (2019) 156001.

[29] G. Gallavotti, Statistical mechanics, texts and monographs in physics (1999).

[30] R. Singh, Ising model, https://rajeshrinet.github.io/blog/2014/ising-model/, accessed: 2023-08-22.

[31] N. Metropolis, A. W. Rosenbluth, M. N. Rosenbluth, A. H. Teller, E. Teller, Equation of state calculations by fast computing machines, The journal of chemical physics 21 (6) (1953) 1087–1092.

[32] I. Seki, K. Nagata, Lattice constant of iron and austenite including its supersaturation phase of carbon, ISIJ international 45 (12) (2005) 1789–1794.

[33] S. Kim, W. Buyers, Vacancy formation energy in iron by positron annihilation, Journal of Physics F: Metal Physics 8 (5) (1978) L103.

[34] Y. Touloukian, T. Makita, Thermophysical properties of matter-the tprc data series. volume 6. specific heat-nonmetallic liquids and gases, Thermophysical and electronic properties information analysis center lafayette in.

[35] J. Piochaud, T. Klaver, G. Adjanor, P. Olsson, C. Domain, C. Becquart, First-principles study of point defects in an fcc fe-10ni-20cr model alloy, Physical review B 89 (2) (2014) 024101.

[36] C. Niu, A. Zaddach, A. Oni, X. Sang, J. Hurt, J. LeBeau, C. Koch, D. Irving, Spin-driven ordering of cr in the equiatomic high entropy alloy nifecrco, Applied Physics Letters 106 (16).

[37] H. e. a. Swanson, International centre for diffraction data (1955).

[38] Z. Rák, D. Brenner, Ab initio investigation of the surface properties of austenitic fe-ni-cr alloys in aqueous environments, Applied Surface Science 402 (2017) 108–113.

[39] Y. Yang, K. G. Field, T. R. Allen, J. T. Busby, Roles of vacancy/interstitial diffusion and segregation in the microchemistry at grain boundaries of irradiated fe–cr–ni alloys, Journal of nuclear materials 473 (2016) 35–53.

[40] A. P. Thompson, H. M. Aktulga, R. Berger, D. S. Bolintineanu, W. M. Brown, P. S. Crozier, P. J. in 't Veld, A. Kohlmeyer, S. G. Moore, T. D. Nguyen, R. Shan, M. J. Stevens, J. Tranchida, C. Trott, S. J. Plimpton, LAMMPS - a flexible simulation tool for particle-based materials modeling at the atomic, meso, and continuum scales, Comp. Phys. Comm. 271 (2022) 108171. doi:10.1016/j.cpc.2021.108171.

[41] M. S. Daw, M. I. Baskes, Embedded-atom method: Derivation and application to impurities, surfaces, and other defects in metals, Phys. Rev. B 29 (1984) 6443–6453. doi:10.1103/PhysRevB.29.6443.
URL https://link.aps.org/doi/10.1103/PhysRevB.29.6443

[42] M. Mendelev, M. Kramer, C. Becker, M. Asta, Analysis of semi-empirical interatomic potentials appropriate for simulation of crystalline and liquid al and cu, Philosophical Magazine 88 (12) (2008) 1723–1750. arXiv:https://doi.org/10.1080/14786430802206482, doi:10.1080/14786430802206482.
URL https://doi.org/10.1080/14786430802206482

[43] G. Bonny, D. Terentyev, R. C. Pasianot, S. Poncé, A. Bakaev, Interatomic potential to study plasticity in stainless steels: the fenicr model alloy, Modelling and Simulation in Materials Science and Engineering 19 (8) (2011) 085008. doi:10.1088/0965-0393/19/8/085008.
URL https://dx.doi.org/10.1088/0965-0393/19/8/085008

[44] M. I. Mendelev, S. Han, D. J. Srolovitz, G. J. Ackland, D. Y. Sun, M. Asta, Development of new interatomic potentials appropriate for crystalline and liquid iron, Philosophical Magazine 83 (35) (2003) 3977–3994. arXiv:https://doi.org/10.1080/14786430310001613264, doi:10.1080/14786430310001613264.
URL https://doi.org/10.1080/14786430310001613264

[45] Y. Mishin, M. J. Mehl, D. A. Papaconstantopoulos, A. F. Voter, J. D. Kress, Structural stability and lattice defects in copper: Ab initio, tight-binding, and embedded-atom calculations, Phys. Rev. B 63 (2001) 224106. doi:10.1103/PhysRevB.63.224106.
URL https://link.aps.org/doi/10.1103/PhysRevB.63.224106

[46] G. Ackland, R. Thetford, An improved n-body semi-empirical model for body-centred cubic transition metals, Philosophical magazine 56 (1987) 15–30. doi:10.1080/01418618708204464.

[47] J. F. Ziegler, The Stopping and Ranges of Ions in Matter: Handbook of Stopping Cross-Sections for Energetic Ions in All Elements, Vol. 5, Elsevier, 2013.

[48] K. Nordlund, Molecular dynamics simulation of ion ranges in the 1–100 kev energy range, Computational Materials Science 3 (4) (1995) 448–456. doi:https://doi.org/10.1016/0927-0256(94)00085-Q.
URL https://www.sciencedirect.com/science/article/pii/092702569400085Q

[49] K. Nordlund, M. Ghaly, R. S. Averback, M. Caturla, T. Diaz de la Rubia, J. Tarus, Defect production in collision cascades in elemental semiconductors and fcc metals, Phys. Rev. B 57 (1998) 7556–7570. doi:10.1103/PhysRevB.57.7556.
URL https://link.aps.org/doi/10.1103/PhysRevB.57.7556

[50] S. Nosé, A unified formulation of the constant temperature molecular dynamics methods, The Journal of Chemical Physics 81 (1) (1984) 511–519. arXiv:https://pubs.aip.org/aip/jcp/article-pdf/81/1/511/9722086/511_1_online.pdf, doi:10.1063/1.447334.
URL https://doi.org/10.1063/1.447334

[51] W. G. Hoover, Canonical dynamics: Equilibrium phase-space distributions, Phys. Rev. A 31 (1985) 1695–1697. doi:10.1103/PhysRevA.31.1695.
URL https://link.aps.org/doi/10.1103/PhysRevA.31.1695

[52] A. Stukowski, Visualization and analysis of atomistic simulation data with ovito–the open visualization tool, Modelling and Simulation in Materials Science and Engineering 18 (1) (2009) 015012. doi:10.1088/0965-0393/18/1/015012.
URL https://dx.doi.org/10.1088/0965-0393/18/1/015012

[53] Crc handbook of chemistry and physics, 84th edition edited by david r. lide (national institute of standards and technology). crc press llc: Boca raton. 2003. isbn 0-8493-0484-9., Journal of the American Chemical Society 126 (5) (2004) 1586–1586. arXiv:https://doi.org/10.1021/ja0336372, doi:10.1021/ja0336372.
URL https://doi.org/10.1021/ja0336372

[54] X. Li, S. Schönecker, J. Zhao, B. Johansson, L. Vitos, Alloying effect on the ideal tensile strength of ferromagnetic and paramagnetic bcc iron, Journal of Alloys and Compounds 676 (2016) 565–574.

[55] B. Gyorffy, A. Pindor, J. Staunton, G. Stocks, H. Winter, A first-principles theory of ferromagnetic phase transitions in metals, Journal of Physics F: Metal Physics 15 (6) (1985) 1337.

[56] X. Li, S. Schönecker, E. Simon, L. Bergqvist, H. Zhang, L. Szunyogh, J. Zhao, B. Johansson, L. Vitos, Tensile strain-induced softening of iron at high temperature, Scientific Reports 5 (1) (2015) 16654.